Ray-tracing-assisted High-Resolution Parameter Estimation for Dynamic Millimeter-Wave Channels

Al-Ameri, Ali; Steinböck, Gerhard; Sanchez, Juan; Tufvesson, Fredrik; Cai, Xuesong

Published in:
19th European Conference on Antennas and Propagation, EuCAP 2025

2025

Document Version:
Peer reviewed version (aka post-print)

Ray-tracing-assisted High-Resolution Parameter Estimation for Dynamic Millimeter-Wave Channels

Ali Al-Ameri*, Gerhard Steinböck† , Juan Sanchez*, Fredrik Tufvesson*, and Xuesong Cai‡*
*Department of Electrical and Information Technology, *Lund University*, Lund, Sweden
†Ericsson Research, *Ericsson AB*, Gothenburg, Sweden
‡School of Electronics, *Peking University*, Beijing, China
{ali.al-ameri, juan.sanchez, fredrik.tufvesson, xuesong.cai}@eit.lth.se gerhard.steinbock@ericsson.com xuesong.cai@pku.edu.cn

***Abstract*—An accurate description of the wireless channel is essential to the development of modern wireless systems. In order to mathematically model the propagation channel, one important prior step often done is high-resolution parameter estimation. The estimation accuracy of this step has a significant impact on how well the channel models can represent reality. In this paper, we address this by improving the estimation performance of the well-known space-alternating generalized expectation maximization algorithm by using ray tracing estimation results in its initialization step. By using the proposed method to estimate multi-path components from raw measurement data gathered from an outdoor measurement campaign, we show that the resulting algorithm gives an improvement in estimation accuracy and lowers computational complexity.**

***Index Terms*—channel parameter estimation, ray tracing, dynamic channels, millimeter-wave (mmWave), and propagation measurements.**

I. Introduction

Propagation research plays a fundamental role in wireless communications. This is because the design and deployment of wireless systems, rely heavily on having a prior understanding of the interaction between the transmitted signals and the physical environment in which they propagate [1]. This is especially true in modern high-frequency wireless systems such as mmWave systems, where achieving high data rates and reliability requires, among other things, well-thought-out deployment scenarios, meticulously designed communication protocols and beamforming techniques – all of which are dependent on prior knowledge of the communication channel.

The behavior of the wireless channel can be studied through different methods that fall primarily into two categories: simulation-based channel characterization and measurement-based channel characterization. *Simulation-based* channel characterization is a convenient way of understanding the wireless channel without conducting measurements [2], [3]. This has its advantages since it removes the need for designing expensive channel sounders. However, it is generally considered a less accurate method compared to the measurement-based approach. This is because simulating complex propagation environments requires simplified assumptions, such as those related to the electromagnetic characteristics of the materials involved in the environment. *Measurement-based* channel characterization, on the other hand, is the dominating way of studying wireless channels in the literature [4], [5]. This is due to the inherent complexity of the real-world propagation mechanisms. This approach is done in three steps. First, channel measurements are carried out with a channel sounder, capturing the raw channel impulse responses. Second, high-resolution parameter estimation (HRPE) is performed on the captured measurement data to estimate the parameters of the multi-path components (MPCs). These parameters include, among others, delays, directions of departure, directions of arrival, and Doppler. Channel modeling is finally conducted based on this parametric information [6].

Consequently, the success of measurement-based channel characterization is highly dependent on the performance of channel parameter estimation. One of the most commonly used HRPE algorithms is the so-called space alternating generalized expectation maximization (SAGE) algorithm [7] that is known for performing well and being computationally efficient. However, one significant drawback is that it is prone to get stuck in local optima, which degrades the performance of parameter estimation. To this end, the contribution of this paper lies in addressing this limitation by combining ray tracing with SAGE to create an improved HRPE algorithm. We do this by first employing ray tracing to get initial estimation results of the parameters for the MPCs in the environment. These ray tracing estimation results are then used to assist the initialization of the SAGE algorithm, leading to improved convergence and parameter estimation accuracy.

The remainder of the paper has the following structure: In Sect. II we introduce the signal model used in this paper and give a quick overview of the SAGE algorithm. In Sect. III we discuss the SAGE algorithm initialization and introduce the ray-tracing-assisted initialization. In Sect. IV we introduce a measurement scenario and present our estimation results using the improved algorithm. Finally, conclusive remarks are included in Sect. V. The notation used in this paper is as

This work has been funded by the Swedish Research Council (Grant No. 2022-04691), the Horizon Europe Framework Programme under the Marie Skłodowska-Curie grant agreement No. 101059091, the Horizon 2020 EU Framework Programme under Grant Agreement No. 861222, the Royal Physiographic Society of Lund, the Strategic Research Area Excellence Center at Linköping–Lund in Information Technology (ELLIIT), and Ericsson.

follows: Bold upper case symbols "**A**" denote matrices and lower case bold symbols "**a**" denote vectors. The operators $(\cdot)^{\mathrm{T}}$ and $(\cdot)^{\mathrm{H}}$ denote transpose and Hermitian operators. The operator $||\cdot||_{\mathrm{F}}$ is the Frobenius norm. Finally, $\otimes$ and $\odot$ denote Kronecker and Hadamard products.

II. Signal model

This section briefly introduces the general signal model for switched array-based channel sounding and an overview of the SAGE algorithm. A representative development of such a sounder is demonstrated in [8].

A. Signal Model

The following case is considered: a switched array multiple-input multiple-output (MIMO) sounder with M_{T} transmit antennas, M_{R} receive antennas and M_{f} frequency points [8]. The received signal $\mathbf{x}(\boldsymbol{\theta}_{\mathrm{sp}}) \in \mathbb{C}^{M\times 1}$ ($M = M_{\mathrm{T}}M_{\mathrm{R}}M_{\mathrm{f}}$) is expressed as a superposition of L MPCs as follows

$$\mathbf{x}(\boldsymbol{\theta}_{\mathrm{sp}}) = \sum_{\ell=1}^{L} \mathbf{A}(\boldsymbol{\theta}_\ell)\cdot\boldsymbol{\alpha}_\ell + \mathbf{z}_\ell, \tag{1}$$

where $\boldsymbol{\alpha}_\ell \in \mathbb{C}^{4\times 1}$ is a vector containing the polarimetric transmission coefficients for the ℓ-th path. The vector $\mathbf{z}_\ell \in \mathbb{C}^{M\times 1}$ denotes the i.i.d white Gaussian noise with a covariance matrix $\mathbf{C} = \sigma^2 I_{M\times M}$. The column vector $\boldsymbol{\theta}_{\mathrm{sp}} = \{\boldsymbol{\theta}_{\boldsymbol{\ell}}, \boldsymbol{\alpha}_{\boldsymbol{\ell}} : l = 1, ..., L\}$ contains the structural parameters for all the paths, while the column vector $\boldsymbol{\theta}_\ell$ contains the parameters for a single path and is defined as

$$\boldsymbol{\theta}_\ell = \begin{bmatrix}\tau_\ell & \nu_\ell & \vartheta_{\mathrm{T},\ell} & \phi_{\mathrm{T},\ell} & \vartheta_{\mathrm{R},\ell} & \phi_{\mathrm{R},\ell}\end{bmatrix}^{\mathrm{T}}. \tag{2}$$

Here, τ_ℓ and ν_ℓ represent the delay and the Doppler frequency of the ℓ-th path. The angles $\vartheta_{\mathrm{R},\ell}$, $\vartheta_{\mathrm{T},\ell}$ represent the elevation of arrival (EOA) and elevation of departure (EOD) for the ℓ-th path. Finally, The angles $\phi_{\mathrm{R},\ell}$, $\phi_{\mathrm{T},\ell}$ are the azimuth of arrival (AOA) and azimuth of departure (AOD). $\mathbf{A}(\boldsymbol{\theta}_\ell) \in \mathbb{C}^{M\times 4}$ is the basis matrix for the ℓ-th path and is defined as

$$\mathbf{A}(\boldsymbol{\theta}_\ell) = \begin{bmatrix} \left[\mathbf{b}_{\mathrm{T_H}}(\phi_{\mathrm{T},\ell},\vartheta_{\mathrm{T},\ell})\otimes\mathbf{b}_{\mathrm{R_H}}(\phi_{\mathrm{R},\ell},\vartheta_{\mathrm{R},\ell})\odot\mathbf{a}(\nu_\ell)\otimes\mathbf{b}_{\mathrm{f}}(\tau_\ell)\right]^{\mathrm{T}} \\ \left[\mathbf{b}_{\mathrm{T_H}}(\phi_{\mathrm{T},\ell},\vartheta_{\mathrm{T},\ell})\otimes\mathbf{b}_{\mathrm{R_V}}(\phi_{\mathrm{R},\ell},\vartheta_{\mathrm{R},\ell})\odot\mathbf{a}(\nu_\ell)\otimes\mathbf{b}_{\mathrm{f}}(\tau_\ell)\right]^{\mathrm{T}} \\ \left[\mathbf{b}_{\mathrm{T_V}}(\phi_{\mathrm{T},\ell},\vartheta_{\mathrm{T},\ell})\otimes\mathbf{b}_{\mathrm{R_H}}(\phi_{\mathrm{R},\ell},\vartheta_{\mathrm{R},\ell})\odot\mathbf{a}(\nu_\ell)\otimes\mathbf{b}_{\mathrm{f}}(\tau_\ell)\right]^{\mathrm{T}} \\ \left[\mathbf{b}_{\mathrm{T_V}}(\phi_{\mathrm{T},\ell},\vartheta_{\mathrm{T},\ell})\otimes\mathbf{b}_{\mathrm{R_V}}(\phi_{\mathrm{R},\ell},\vartheta_{\mathrm{R},\ell})\odot\mathbf{a}(\nu_\ell)\otimes\mathbf{b}_{\mathrm{f}}(\tau_\ell)\right]^{\mathrm{T}} \end{bmatrix}^{\mathrm{T}} \tag{3}$$

where $\mathbf{b}_{\mathrm{T_H}}(\phi_{\mathrm{T},\ell},\vartheta_{\mathrm{T},\ell}) \in \mathbb{C}^{M_{\mathrm{T}}\times 1}$, $\mathbf{b}_{\mathrm{T_V}}(\phi_{\mathrm{T},\ell},\vartheta_{\mathrm{T},\ell}) \in \mathbb{C}^{M_{\mathrm{T}}\times 1}$ are the transmitter (Tx) array responses for the horizontal and vertical polarization respectively, while $\mathbf{b}_{\mathrm{R_H}}(\phi_{\mathrm{R},\ell},\vartheta_{\mathrm{R},\ell}) \in \mathbb{C}^{M_{\mathrm{R}}\times 1}$, and $\mathbf{b}_{\mathrm{R_V}}(\phi_{\mathrm{R},\ell},\vartheta_{\mathrm{R},\ell}) \in \mathbb{C}^{M_{\mathrm{R}}\times 1}$ are the receiver (Rx) array responses. It is worth noting that both the Tx and Rx array responses are obtained using the effective aperture distribution function (EADF) based on the characterization of antenna arrays in an anechoic chamber [9]. The vector $\mathbf{a}(\nu_\ell) \in \mathbb{C}^{M_{\mathrm{T}}M_{\mathrm{R}}\times 1}$ describes the Doppler-induced phase shift caused by the dynamic channel. Finally, $\mathbf{b}_{\mathrm{f}}(\tau_\ell) \in \mathbb{C}^{M_{\mathrm{f}}}$ is the delay-dependent frequency basis vector. Readers are also referred to [10] for more details.

B. SAGE Algorithm

SAGE is a maximum-likelihood-based iterative algorithm, with an estimation uncertainty that can approach the Cramer-Rao lower bound with much lower complexity [7], [11]. It is extended upon the expectation-maximization (EM) algorithm that contains the expectation (E)-step and the maximization (M)-step in the iterative procedure. Briefly, in the E-step of the k-th iteration, the complete data for the ℓ-th path, $\hat{\mathbf{y}}_{\ell,k}$, is obtained as

$$\hat{\mathbf{y}}_{\ell,k} = \mathbf{A}(\boldsymbol{\theta}_{\ell,k})\cdot\boldsymbol{\alpha}_{\ell,k} + \beta_\ell\left(\mathbf{x}(\boldsymbol{\theta}_{\mathrm{sp}}) - \sum_{n=1}^{L}\mathbf{A}(\boldsymbol{\theta}_{n,k})\cdot\boldsymbol{\alpha}_{n,k}\right) \tag{4}$$

and in the M-step, the channel parameters are updated as

$$\boldsymbol{\theta}_{\ell,k+1} = \arg\max_{\boldsymbol{\theta}} \hat{\mathbf{y}}_{\ell,k}^{\mathrm{H}}\mathbf{A}(\boldsymbol{\theta})\left(\mathbf{A}^{\mathrm{H}}(\boldsymbol{\theta})\mathbf{A}(\boldsymbol{\theta})\right)^{-1}\hat{\mathbf{y}}_{\ell,k}, \tag{5}$$

$$\boldsymbol{\alpha}_{\ell,k+1} = \left(\mathbf{A}^{\mathrm{H}}(\boldsymbol{\theta}_{\ell,k+1})\mathbf{A}(\boldsymbol{\theta}_{\ell,k+1})\right)^{-1}\mathbf{A}^{\mathrm{H}}(\boldsymbol{\theta}_{\ell,k+1})\hat{\mathbf{y}}_{\ell,k}. \tag{6}$$

This iterative procedure continues until convergence or a predefined number of iterations is reached. The SAGE algorithm further decreases the complexity of EM by decomposing the estimation in (4)-(6) into several lower-dimensional (or single-dimensional) optimization problems and updating the parameters immediately after estimation.

III. Initialization

In this section, the initialization procedure and the use of ray tracing to improve the initialization step are discussed.

A. Successive Interference Cancellation

A typical way of performing the initialization of SAGE is through successive interference cancellation. Specifically, for the first iteration, it is assumed that all the path parameters are zero. Thus, the complete data for the ℓ-th path reduces to

$$\hat{\mathbf{y}}_{\ell,0} = \mathbf{x}(\boldsymbol{\theta}_{\mathrm{sp}}) - \sum_{n=1}^{l-1}\mathbf{A}(\boldsymbol{\theta}_{n,0})\cdot\boldsymbol{\alpha}_{n,0}. \tag{7}$$

After this, the path parameters of the current path are updated in the M-step in the same fashion as in (5)-(6). This initialization works by solving the maximization problem in (5)-(6), for each path, by searching among a large set of parameter candidates to maximizes the likelihood. The set of parameter candidates to search among has to be sufficiently large, the reason for this is because initially, there is no prior information about what parameters to expect. For example, the set of RX azimuth candidates can be between 0° and 360° with steps of 6°.

B. Ray-tracing-assisted Initialization

As noted in the previous subsection, the described initialization method does not have prior information about the initial path parameters. Performing initialization in such a blind way implies a computationally expensive search among a large set of parameter candidates. Another disadvantage of the described initialization method is that it performs the

maximization based on the data decomposition (5), which is highly prone to getting stuck in local maxima. One common reason is the imperfect sounder calibration, which is practically inevitable. In this case, the algorithm can be stuck in the residual ("ghost") components of high-power paths, making it difficult to go to other paths with weaker powers.

We propose to improve this by using prior data to get these initial values. Specifically, we achieve this with ray tracing simulations of the MPCs, and we call the resulting algorithm ray-tracing-initialized space-alternating generalized expectation maximization (R-SAGE). First, the ray tracing results of MPCs are generated. Then the geometry parameters of MPCs obtained in ray tracing are considered initial values for the SAGE algorithm to search among a reduced set of candidates around the results predicted by ray tracing. This reduces the search complexity of (5) significantly and also makes it less prone to getting stuck in local maxima, leading to more accurate estimation.

IV. Results

This section introduces an outdoor measurement campaign and the ray tracer used to generate the MPCs in the measurement scenario. The performance difference between SAGE and the proposed R-SAGE algorithm is compared.

A. Measurement Campaign

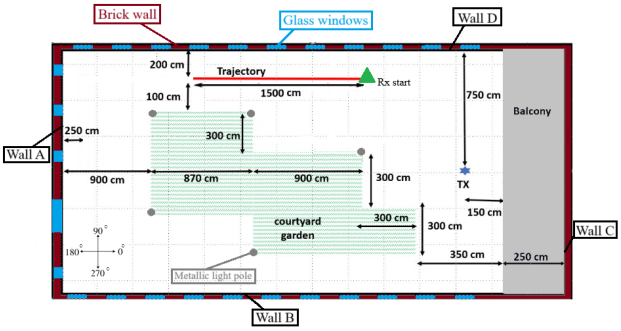

(a) 2D sketch of the measurement environment.

(b) Real-life image of the measurement environment.

Fig. 1: Measurement environment.

The measurement was conducted in a courtyard as shown in Fig. 1, which is enclosed by brick walls and several glass windows with metallic frames. At the center of the courtyard, there is a small garden surrounded by metallic light poles. The courtyard dimensions are $35.75 \times 15\,\mathrm{m}^2$. The propagation channels were measured using a mmWave dual polarized switched array sounder [8]. The Tx is a flat rectangular array with 128 antenna ports, while the Rx is an octagonal array with 256 antenna ports. The sounder operates at a center frequency of 28 GHz and has a bandwidth of 768 MHz, giving a delay resolution of around 0.4 meters. As shown in Fig. 1a, Tx array is marked with a blue star and faces wall A. The Rx was moved along a trajectory marked with a red line in steps of 10 cm, with the start position marked with a green triangle. More details about the measurement campaign can be found in [12].

B. Ray tracing Settings

For the described measurement campaign a 3D model is created for the ray tracing tool. The 3D model is based on manual measurements, see Fig. 1, and the recorded LiDAR 3D point cloud [12]. Based on the LiDAR data, details such as wedges around windows and doors are included. Different materials are assigned to ground, walls, windows, etc. based on material properties specified in [13]. Based on the LiDAR data, objects such as cylindrical light poles and tree trunks are also included in the 3D model. The ray tracing tool considers various propagation mechanisms. Specular reflections and transmissions are based on the Fresnel coefficients [13]. The uniform theory of diffraction (UTD) is implemented for wedge structures based on [14], [15]. Lambertian diffuse scattering model [16], [17], which corrects for surface roughness, back scattering due to small-scale geometric variations over the surfaces, etc., is also implemented. The scattering from cylindrical objects is described in [18].

The settings for interaction type combinations of these particular simulations are as follows: A maximum order of interactions per simulated path is chosen to be 6. Limited by this maximum order, any number and combination of up to 6 specular reflections, up to 1 diffraction, and up to 1 cylindrical scattering interaction are allowed. Diffuse scattering is not considered. The electromagnetic properties of the materials are based on [13]. The brick wall is chosen to be a layered material of 12 cm ITU bricks, and 15 cm ITU concrete. The window is layered as 8 mm ITU glass, 6 mm air, and 8 mm ITU glass. The concrete structures such as the balcony are modeled as 30 cm ITU concrete. Finally, the ground is modeled as concrete with thickness of the radius of the earth.

C. Estimation Results and Comparison

Figs. 2-4 illustrate the channel parameter estimation results for the measurement data, using SAGE and the proposed ray-tracing-initiated SAGE, i.e., the R-SAGE algorithm. In these figures, estimation results of SAGE and R-SAGE are compared by plotting the 60 strongest paths estimated at each Rx position along the trajectory marked in Fig. 1.

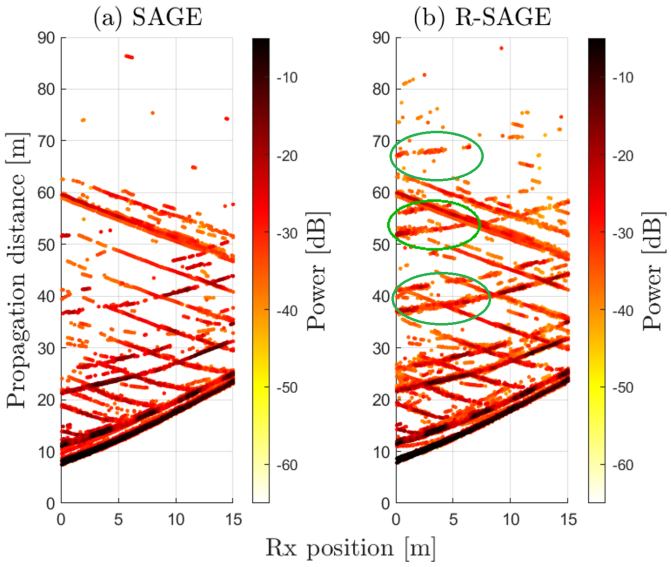

Fig. 2: Propagation distance plotted over different Rx positions along its trajectory. (a) Using SAGE. (b) Using R-SAGE.

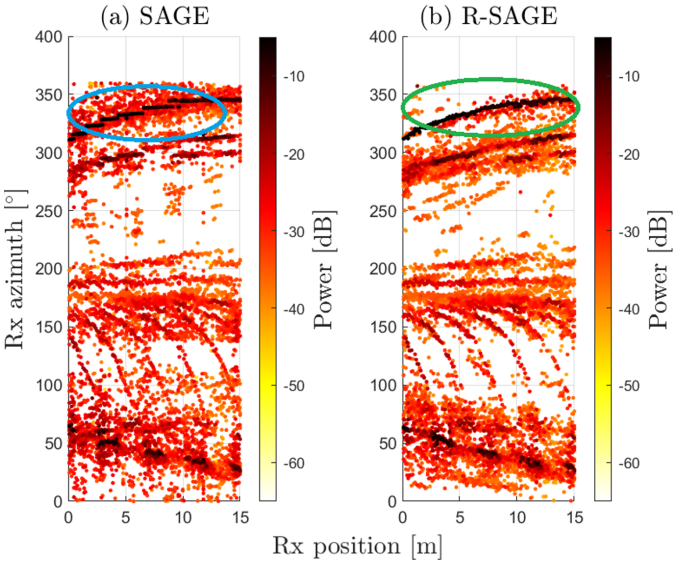

Fig. 3: Rx azimuth angles plotted over different Rx positions along its trajectory. (a) Using SAGE. (b) Using R-SAGE.

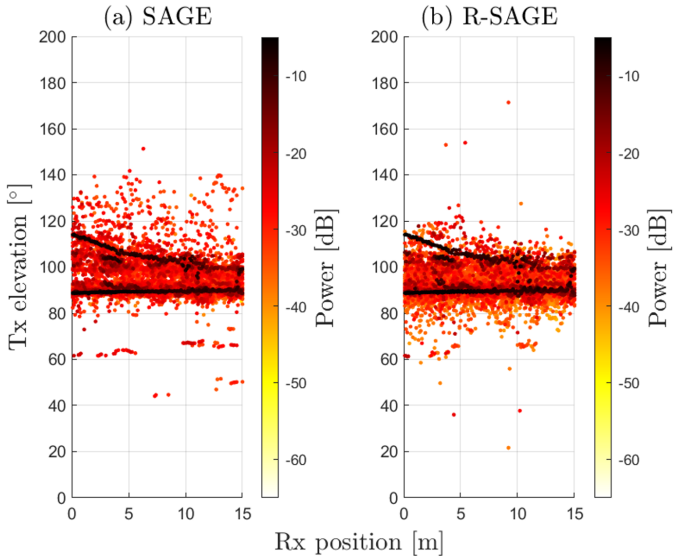

Fig. 4: Tx elevation angles plotted over different Rx positions along its trajectory. (a) Using SAGE. (b) Using R-SAGE.

Fig. 2 illustrates the delay comparison. By closely examining Fig. 2(a) and (b), one can notice that the delay estimation results of both SAGE and R-SAGE are extremely similar for the most part. This indicates that R-SAGE reduces the initialization complexity significantly by decreasing the search area exploiting the ray tracing results at no cost of estimation performance for those paths. It can also be observed that R-SAGE improves the estimation performance for other paths. As highlighted by the green circles in Fig. 2(b), several new path trajectories can be identified, and many paths are much more continuous. Overall, the paths in Fig. 2(b) are easier to track across snapshots compared to Fig. 2(a). The improvement observed in Fig. 2 is also present in Fig. 3, where the Rx azimuth estimation results are compared. Additionally, by inspecting the highlighted blue circle in Fig. 3(a), it can be observed that there is a "stepping" behavior present. This is due to ambiguities in the angular estimation caused by the sequential switching sequences of the switched sounder used in the measurement, which has been investigated in [10], [19]. As shown in the green circle in Fig. 3(b), it is noticeable that this stepping behavior does not occur when using R-SAGE. As the search area in the initialization with R-SAGE is significantly reduced, selecting an ambiguity is less likely. This is another benefit of the proposed method. Finally, Fig. 4 illustrates the comparison between the estimation results of Tx elevation. It can be observed in Fig. 4(b) that R-SAGE gives more "concentrated" estimation results between around 90° and 115°.

The above figures highlight that the parameter estimation is improved when assisted by ray tracing. On the one hand, it decreases the complexity while maintaining the parameter estimation performance of most paths. On the other hand, it helps the algorithm find paths that otherwise cannot be effectively found before due to, e.g., imperfect calibrations.

V. Conclusions

In this paper, we proposed an improved SAGE algorithm using the ray tracing data for enhanced initialization. By applying the proposed algorithm to a set of measurement data gathered from an outdoor measurement campaign, we showed that the proposed algorithm gives improved parameter estimation performance compared to regular SAGE. For future work, one can notice that the ray tracer may not fully capture all the multipath components in the real channels. Thus, it is worth combining the R-SAGE with regular SAGE to ensure that all the paths are well-initialized and estimated from the measurement data. Another direction is that the path estimate results from R-SAGE could be fed back into the ray tracing tool to improve the accuracy of the ray tracer, especially

regarding path amplitudes.

REFERENCES

[1] X. Cai, X. Cheng, and F. Tufvesson, "Toward 6G with terahertz communications: Understanding the propagation channels," *IEEE Communications Magazine*, vol. 62, no. 2, pp. 32–38, 2024.

[2] L. Tian *et al.*, "Semi-deterministic radio channel modeling based on graph theory and ray-tracing," *IEEE Transactions on Antennas and Propagation*, vol. 64, no. 6, pp. 2475–2486, 2016.

[3] E. M. Vitucci *et al.*, "Polarimetric properties of diffuse scattering from building walls: Experimental parameterization of a ray-tracing model," *IEEE Transactions on Antennas and Propagation*, vol. 60, no. 6, pp. 2961–2969, 2012.

[4] J. Gomez-Ponce *et al.*, "Directionally resolved measurement and modeling of THz band propagation channels," *IEEE Open Journal of Antennas and Propagation*, vol. 3, pp. 663–686, 2022.

[5] A. Al-Ameri *et al.*, "A fast rotating-mirror sounder for dynamic millimeter-wave channel characterization," in *Proc. IEEE 100th Vehicular Technology Conference (VTC2024-Fall)*, 2024, pp. 1–5.

[6] Z. Huang *et al.*, "A mixed-bouncing based non-stationarity and consistency 6G V2V channel model with continuously arbitrary trajectory," *IEEE Transactions on Wireless Communications*, vol. 23, no. 2, pp. 1634–1650, 2024.

[7] B. Fleury *et al.*, "Channel parameter estimation in mobile radio environments using the SAGE algorithm," *IEEE Journal on Selected Areas in Communications*, vol. 17, no. 3, pp. 434–450, 1999.

[8] X. Cai *et al.*, "A switched array sounder for dynamic millimeter-wave channel characterization: Design, implementation and measurements," *IEEE Transactions on Antennas and Propagation*, vol. 72, no. 7, pp. 5985–5999, 2024.

[9] ——, "Enhanced effective aperture distribution function for characterizing large-scale antenna arrays," *IEEE Transactions on Antennas and Propagation*, vol. 71, no. 8, pp. 6869–6877, 2023.

[10] A. Al-Ameri *et al.*, "A hybrid antenna switching scheme for dynamic channel sounding," in *IEEE 97th Vehicular Technology Conference (VTC2023-Spring)*, 2023, pp. 1–6.

[11] B. Fleury *et al.*, "Wideband angle of arrival estimation using the SAGE algorithm," in *Proceedings of ISSSTA'95 International Symposium on Spread Spectrum Techniques and Applications*, vol. 1, 1996, pp. 79–85 vol.1.

[12] H. Khosravi, X. Cai, and F. Tufvesson, "Experimental analysis of physical interacting objects of a building at mmWave frequencies," in *18th European Conference on Antennas and Propagation (EuCAP)*, 2024, pp. 1–5.

[13] "Effects of building materials and structures on radiowave propagation above about 100 MHz," *Recommendation ITU-R P.2040-2*, 2021.

[14] D. A. McNamara, C. W. Pistorius, and J. Malherbe, *Introduction to the uniform geometrical theory of diffraction*. Artech House Norwood, MA, 1990.

[15] R. Kouyoumjian and P. Pathak, "A uniform geometrical theory of diffraction for an edge in a perfectly conducting surface," *Proceedings of the IEEE*, vol. 62, no. 11, pp. 1448–1461, 1974.

[16] V. Degli-Esposti, "A diffuse scattering model for urban propagation prediction," *IEEE Transactions on Antennas and Propagation*, vol. 49, no. 7, pp. 1111–1113, 2001.

[17] V. Degli-Esposti *et al.*, "Measurement and modelling of scattering from buildings," *IEEE Transactions on Antennas and Propagation*, vol. 55, no. 1, pp. 143–153, 2007.

[18] R. Heijs *et al.*, "On the importance of scattering from poles in ray tracing simulations," in *18th European Conference on Antennas and Propagation (EuCAP)*, 2024, pp. 1–5.

[19] R. Wang *et al.*, "Antenna switching sequence design for channel sounding in a fast time-varying channel," in *IEEE International Conference on Communications (ICC)*, 2018, pp. 1–6.